PET Imaging of Solid Tumors with A G-quadruplex-targeting ^{18}F-Labelled Peptide Probe

Xiao-Chun Guo[1,†], Da-Zhi Shi[2,†], Shun Huang[3,*], Yi-Han Zhang[1], Wan-Ying Zhang[1], Jing Chen[1], Zebin Huang[1], Hubing Wu[2], Jin-Qiang Hou[4,6], Fu-Jun Jin[1], Xiu-Cai Chen[1], Wing-Leung Wong[5], Yu-Jing Lu[1,7,*]

[1] Guangdong Medicine-Engineering Interdisciplinary Technology Research Center, School of Biomedical and Pharmaceutical Sciences, Guangdong University of Technology, Guangzhou 510006, China.

[2] Department of Nuclear Medicine, Nanfang Hospital, Southern Medical University, Guangzhou 510515, China.

[3] Department of Nuclear Medicine, The Tenth Affiliated Hospital, Southern Medical University (Dongguan People's Hospital), Dongguan 523059, China.

[4] Department of Chemistry, Lakehead University, 955 Oliver Road, Thunder Bay, Ontario P7B 5E1, Canada.

[5] State Key Laboratory of Chemical Biology and Drug Discovery, Department of Applied Biology and Chemical Technology, The Hong Kong Polytechnic University, Hung Hom, Kowloon, Hong Kong SAR 999077, China.

[6] Thunder Bay Regional Health Research Institute, 980 Oliver Road, Thunder Bay, Ontario P7B 6V4, Canada.

[7] Smart Medical Innovation Technology Center, Guangdong University of Technology, Guangzhou 510006, China.

[†] These authors contributed equally to this paper.

* Corresponding author.

E-mail (SH): shunhuang007@163.com

E-mail (YJL): luyj@gdut.edu.cn

ABSTRACT: Positron emission computed tomography (PET) is a common imaging technique and can provide accurate information about the size, shape and location of tumors. Recent evidence has shown that G-quadruplex structures (G4s) are identified in human oncogenes and these special structures are recognized as diagnostic cancer markers and drug targets for anticancer therapies. Although a number of techniques for *in vivo* imaging of G4s have been developed, achieving of sufficient sensitivity and selectivity *in vivo* remains challenging. Herein, we have engineered and developed a radiolabelled peptide probe [^{18}F]AlF-NOTA-RHAU18 targeting mitochondrial DNA G4s for *in vivo* PET imaging. The results of the study indicate that this probe is able to visualize and detect solid tumors in living homozygous mice. In addition, the distribution of the probe in cancer cells was investigated using FITC-RHAU18. This work may offer new insights into the development of cancer diagnostic tools by targeting *in vivo* G4s.

Keywords G-quadruplex; PET/CT imaging; peptide probe; NOTA; solid tumor

INTRODUCTION

The G-quadruplex structure (G4) is an atypical nucleic acid secondary structure formed by the folding of guanine-rich DNA or RNA, in which four guanines form a G-quartet via Hoogsteen hydrogen bonding interactions and two or more of these G-quartets undergo self-stacking to form a G4[1]. G4s can be further stabilized by chelating metal cations such as potassium ion in the central channel[2]. G4s are generally classified into parallel, antiparallel, and hybrid structures depending on their folding patterns. Shankar's group recently reported that G4 structure-forming regions (ΔG4Rs) were enriched in breast cancer patient-derived tumor xenograft models and associated with the promoters of highly amplified genes with high level of expression[3]. Genome-wide bioinformatic analyses reveal that the human genome contains over 700,000 G-rich sequences capable of forming G-quadruplexes, which are commonly found in the region of oncogene promoters and telomeres[4]. Several studies have demonstrated that G4s play vital roles in the essential biological processes including gene replication, translation and transcription regulation, and chromosomal recombination maintenance[5]. G4s are thus regarded as promising targets for chemical biology and anticancer research[6]. Taken together, the enrichment of G4s in proto-oncogenes highlights their potential as promising

targets for the development of cancer diagnostics[7].

Over the past decade, researchers have developed an array of ligands by rational design to achieve high selectivity targeting G4s and to facilitate *in vitro* studies of G-quadruplexes and their visualization in living cells[8-12]. Currently, the use of target-selective small-molecule fluorescent probes and target-specific G4 antibodies are the two primary tools to investigate G4s *in vitro* and *in cellulo*. Some small-molecule fluorescent probes were reported capable of recognizing a specific type or class of G4s. For instance, BMVC[13] targets telomeric G4s, L-PDS[14] identifies DNA G4s, MitoISCH[12] targets mitochondrial DNA G4s, while QUMA-1[9] and CyT[15] recognize RNA G4s. Nevertheless, the excitation wavelength of most small-molecule fluorescent probes is not able to penetrate the skin deeply and may pose toxicity to cells. Thus, these limitations largely hinder their applications *in vivo*. In addition, target-specific antibodies such as BG4[8], 1H6[16], and G4P[10] have been developed to detect G4s. However, the application of G4-antibodies is limited as they are primarily employed in the immune-based techniques such as immunofluorescence and immunoblotting.

In addition, there are certain limitations in using small-molecule fluorescent probes or G4-antibodies for visualizing G4s *in vivo*. Therefore, it is desired to develop a more advanced biosensing technology for the study of *in vivo* G4s. To design G4-targeting peptides is a new strategy. Furthermore, small peptides may be less immunogenic and easier to be designed and synthesized compared with proteins[17].

At present, some G4s binding proteins have been reported and DEAH-box helicase RHAU is one of the notably examples. RHAU specifically binds to parallel G4s and regulates G4-folding/unfolding process *in vivo* with a unique ATP-dependent deconjugating enzyme activity[18]. The N-terminus of RHAU was found required for RHAU to unwind G4s. Moreover, the N-terminal RSM fragment was found an essential binding structural domain for recognizing and binding to G4s[19]. In the present study, we demonstrated that the peptides derived from RHAU could be morphed into G4-binding ligands to achieve high specificity and sensitivity targeting G4s. Thus, these newly developed G4-sensing peptides are potential candidates for *in vivo* visualization and therapeutic intervention targeting G4s.

Positron emission computed tomography (PET) is a widely used molecular imaging technique and provides accurate information about the size, shape and location of tumors by

imaging the metabolic activity of specific probes at cellular or molecular level. PET imaging technique can provide imaging support for accurate diagnosis, staging and treatment planning[20]. Thus, we designed an ^{18}F-labeled PET peptide probe, [^{18}F]AlF-NOTA-RHAU18, that was primarily localized in mitochondria and binding to parallel DNA G4-structures *in cellulo* and *in vivo*. The signal enrichment of [^{18}F]AlF-NOTA-RHAU18 at tumor sites was successfully demonstrated in living homozygous mice and revealed a preferential binding of the probe to mitochondrial G4s.

RESULTS AND DISCUSSION

Design and radiosynthesis of a G4-binding PET peptide probe. Several regions selected from RHAU were studied for their interaction with G4s and it was found that the N-terminal RSM fragment (13 amino acids) was essential for recognizing and binding to G4s[18]. However, excessively long peptides hinder their potential as desirable drugs[21]. Considering that shortening the peptide by reducing the number of amino acids in the sequence may result in a loss of binding ability and selectivity due to losing secondary structure, we therefore virtually screened various small regions of RHAU and identified an 18-amino-acid peptide, RHAU18 (sequence: HPGHLKGREIGMWYAKKQ), which included a RSM fragment, for G4-probe design and modification.

To label a peptide with the radionuclide fluorine-18, we adopted an Al[^{18}F]F labelling method by coupling the chelator NOTA to the peptide chain and then using Al[^{18}F]F to bind to the chelator NOTA for radioactivity detection[22]. Based on molecular docking results obtained, the first amino acid, histidine, at the N-terminal end of RHAU18 has relatively low spatial resistance and it does not directly participate in interactions with nucleic acids[23]. It is therefore an ideal site for coupling NOTA. The radiolabeling of NOTA-RHAU18 was carried out with the mixture of $AlCl_3$ and NaOAC buffer (Supplementary Scheme S1)[24]. The non-decay corrected labeling yield of [^{18}F]AlF-NOTA-RHAU18 was 19.5 ± 3.9% (n = 10). The molar activities of [^{18}F]AlF-NOTA-RHAU18 was 14.9 ± 3.3 GBq/μmol (n = 10). The purity of [^{18}F]AlF-NOTA-RHAU18 determined with HPLC was over 99% (Supplementary Figure S1 and S4). The partition coefficient (logP) of [^{18}F]AlF-NOTA-RHAU18 was -3.13 ± 0.06, indicating its good hydrophilicity. Moreover, the results of stability study shown in

Supplementary Figure S5 revealed that [^{18}F]AlF-NOTA-RHAU18 in PBS, serum, blood and urine *in vivo* showed no significant decompositions during the observation period. The results may indicate that probe was stable *in vitro* and *in vivo* and it could be feasible to visualize [^{18}F]AlF-NOTA-RHAU18 *in vivo*. To avoid nuclear contamination, the *in vitro* evaluation was performed with [^{19}F]AlF-NOTA-RHAU18 instead of [^{18}F]AlF-NOTA-RHAU18 (Supplementary Figure S2).

Evaluation of RHAU18 as a parallel G-quadruplex probe *in vitro*. To investigate the ability of peptides coupled to the NOTA loop binding to G4s *in vitro*, we first determined the T_m values of a parallel G4, pu22, before and after incubation with the peptide using CD melting experiments. The T_m of pu22 was 69.49 °C. After incubation with an equimolar amount of RHAU18, the T_m increased to 75.52 °C. After incubation with NOTA-RHAU18, T_m was further increased to 76.82 °C (Figure 1a). These results indicate that both RHAU18 and NOTA-RHAU18 are able to interact with pu22 and stabilize the G4-structure formed.

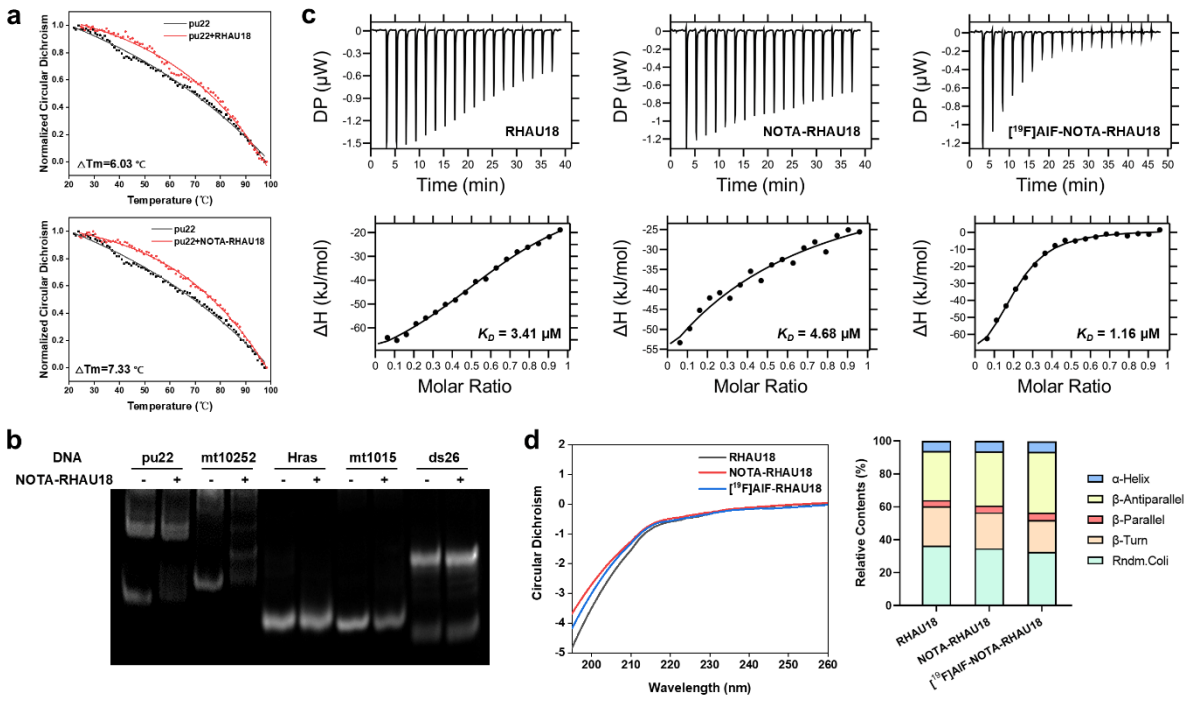

Figure 1. (a) Melting point change of pu22 (5 μM) after binding with RHAU18 and NOTA-RHAU18 (10 μM). Buffer: Tris-HCl (10 mM, pH 7.5) containing 60 mM KCl. (b) Electrophoretic mobility shift assay for DNA binding. Different types of nucleic acids (5 μM) were subjected to electrophoresis with or without co-incubation with NOTA-RHAU18 (100 μM), and stained with SYBR Gold for imaging. (c) Isothermal titration calorimetry profile of peptides binding to pu22. (d) Circular dichroism spectroscopy of aqueous solutions of RHAU18 (black), NOTA-RHAU18 (red) and [^{19}F]AlF-RHAU18 (blue), and relative contents

(%) of particular secondary structures of peptides, as elucidated by analyzing the CD spectroscopy with CDNN.

Subsequently, electrophoretic mobility shift assays were conducted using NOTA-RHAU18 with parallel G4s (pu22, mt10252), anti-parallel G4 (Hras), hybrid G4 (mt1015), and double-stranded DNA (ds26). The electropherograms show that parallel G4s exhibited significant hysteresis after incubation with NOTA-RHAU18 compared to the nucleic acid substrate alone, whereas non-parallel G4s and double-stranded nucleic acids do not show such changes (Figure 1b).

To verify further the binding property of the peptide to different types of nucleic acids, the thermodynamic and kinetic information of the mixture of the peptide and nucleic acids were obtained using isothermal titration microcalorimetry. The parallel G4s (pu22, CKIT2, Bcl2, 22RT, VEGF22 and mt10252) showed better binding ability, and the K_D values were in the micromolar range (Figure 1c, Table S3-S5, and Supplementary Figure S6-S8). These results demonstrate that the coupling of RHAU18 to NOTA does not alter its selectivity toward parallel G4s. In addition, by analyzing the relative content of specific secondary structures of the peptide elucidated by CD spectroscopy using CDNN software, the content of various secondary structures (α-Helix, β-Antiparallel, β-Parallel, β-Turn and Rndm.Coli) of NOTA-RHAU18 and [^{19}F]AlF-NOTA-RHAU18 was not markedly altered with respect to RHAU18 (Figure 1d)[25]. The results demonstrate that NOTA-RHAU18 may retain the same secondary structure as RHAU18.

Evaluation of RHAU18 as a parallel G-quadruplex probe in cells. Previous *in vitro* studies demonstrated that RHAU18 and its fluorine chelator exhibited a high selectivity toward parallel G4s. In the subsequent study, we investigated the cellular distribution and the target of RHAU18 by substituting the coupled NOTA with FITC (Supplementary Figure S3). First, enzymatic digestion experiments were conducted. For DNase I treatment, almost all FITC-RHAU18 foci were disappeared, while there were negligible changes found in the fixed human hepatocellular carcinoma cells (Huh7) after RNase A treatment. The results indicate that FITC-RHAU18 primarily binds to DNA (Figure 2a). To confirm the binding of FITC-RHAU18 to G4s, we applied a potent and non-emissive G4-ligand, BRACO19[26], at different concentrations to compete with FITC-RHAU18 in fixed Huh7 cells. It was found that the green fluorescent

foci (FITC-RHAU18) were gradually diminished as the concentration of BRACO19 increased (Figure 2b).

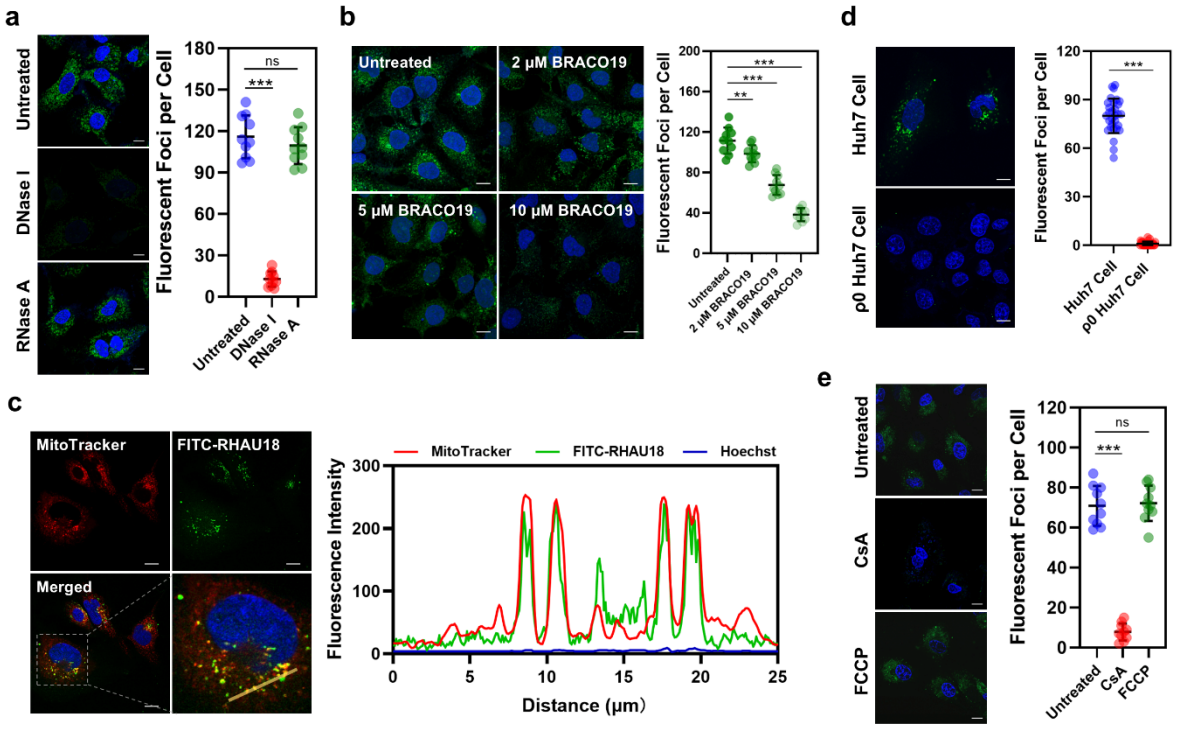

Figure 2. (a) Fixed Huh7 cells were treated by DNase I or RNase A and stained with 5 μM FITC-RHAU18 (green). The nucleus was visualized by Hoechst33342 (blue). (b) Fixed Huh7 cells were stained with FITC-RHAU18 and then cells were treated with different concentrations of BRACO19 to displace the ligand. (c) Live Huh7 cells were stained with 10 μM FITC-RHAU18 and the mitochondria are indicated by Mito Tracker (red). Enlarged images in the dotted line regions and relative fluorescence intensity profiles across the yellow line inside are shown in right panel. (d) Live Huh7 cells and ρ0 Huh7 cells were stained with 10 μM FITC-RHAU18 for 2 h. For each sample of cell image, 30 cells were measured. The data are presented as mean ± SEM, and statistical significance is determined by the t test as (ns) not significant, (*) $P < 0.05$, (**) $P < 0.01$, and (***) $P < 0.001$. Scale bars for cell image: 10 μm. (e) Confocal images of live Huh7 cells stained with 10 μM FITC-RHAU18 for 30 min and 1 μM Hoechst33342 for 15 min after treatment with FCCP or CsA.

In the co-localization study of FITC-RHAU18 with organelle-specific dyes, we observed a high degree of co-localization between FITC-RHAU18 and the mitochondrial dye MitoTracker, suggesting that the target of FITC-RHAU18 could be mitochondrial DNA (mtDNA) (Figure 2c). To further clarify that the target of FITC-RHAU18 is mtDNA in the cells, the mtDNA-depleted ρ0-Huh7 cells were constructed and then were utilized for cell-imaging with FITC-RHAU18[27]. Unlike in parental Huh7 cells, the deletion of mtDNA in ρ0-Huh7 cells resulted in a complete loss of FITC-RHAU18 foci (Figure 2d), indicating that FITC-RHAU18 interacts with mtDNA in live Huh7 cells.

We further explored the mechanism of FITC-RHAU18 entering into mitochondria. Small molecules or peptides can enter mitochondria via the mitochondrial permeability transition pore (mPTP). The blocking of mPTP can prevent them from getting into the mitochondrial matrix. Additionally, positively charged compounds are typically mitochondria-targeting because of the negative mitochondrial membrane potential (MMP). Using cyclosporin A (CsA)[28], an mPTP inhibitor, to block mPTP of the cells, the green fluorescent foci of FITC-RHAU18 in the cells was significantly reduced. However, the depolarization of MMP of Huh7 cells using a mitochondrial uncoupling agent, carbonyl cyanide 4-(trifluoromethoxy)phenylhydrazone (FCCP)[29], did not markedly alter the fluorescent foci (Figure 2e). These results suggest that FITC-RHAU18 is primarily delivered to intracellular mitochondria through the mitochondrial permeability transition pore.

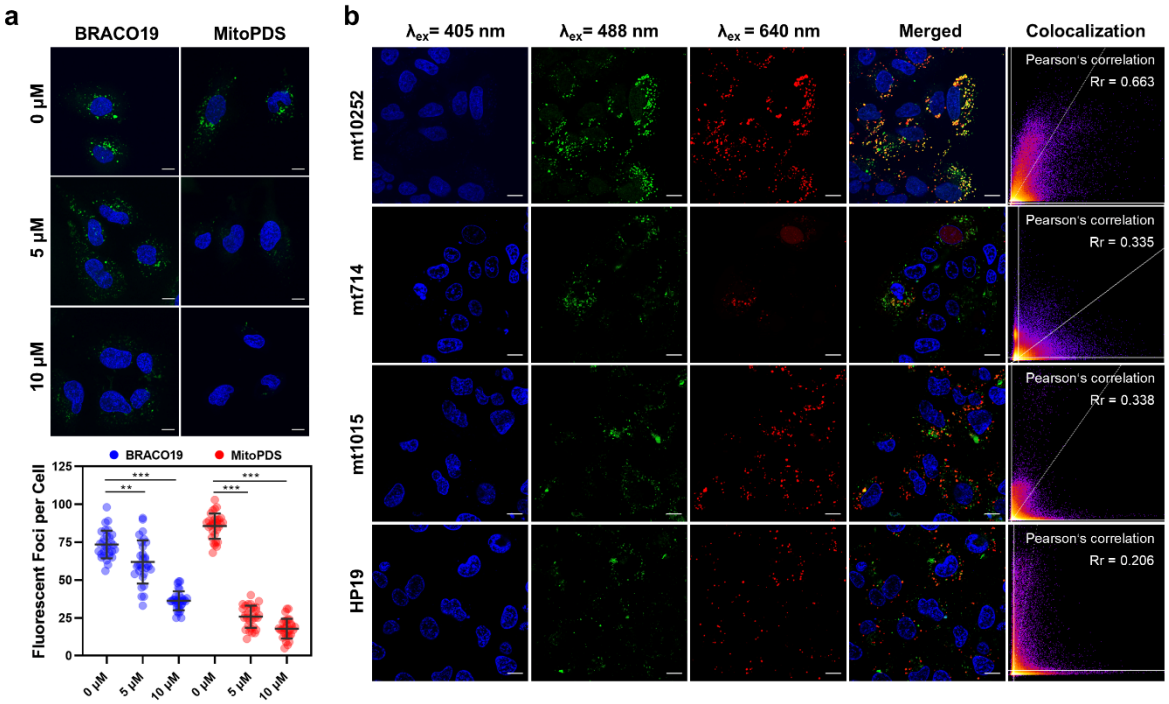

Figure 3. (a) Live Huh7 cell cells were treated with different concentrations of BRACO19 or MitoPDS, and then competitively stained with FITC-RHAU18 for 2 h. (b) Confocal images for the co-localization analysis. Living Huh7 cells were transfected with Cy5-coupled mt10252, mt714, mt1015 and HP19 for 24 h and then stained with FITC-RHAU18 for 2 h and Hoechst33342 for 15 min. For each sample of cell image, 30 cells were measured. The data are presented as mean ± SEM, and statistical significance is determined by the t test as (ns) not significant, (*) $P < 0.05$, (**) $P < 0.01$, and (***) $P < 0.001$. Scale bars for cell image: 10 µm.

Next, we aimed to determine the selectivity of FITC-RHAU18 targeting G4s in cells. We performed intracellular competition assays for FITC-RHAU18 with two well-known G4-ligands including non-emissive BRACO19 and mtDNA G4-targeting MitoPDS[12]. Firstly, the Huh7 cells were treated separately with these two G4-ligands overnight. Then, the cells were imaged after being treated with FITC-RHAU18. We observed that the green foci of FITC-RHAU18 were significantly reduced after the treatment with BRACO19 at 5 µM compared to the control group. An even greater reduction was observed for the cells treated with 10 µM BRACO19. Moreover, the results were found more pronounced in cells treated with MitoPDS that was mtDNA G4-targeting. The green foci almost completely disappeared after treatment with MitoPDS at 5 µM (Figure 3a). The competition experiments demonstrate that these reported potent G4-ligands may occupy G4-targets in the cells and thus it hinders FITC-RHAU18 binding to these targets. In other words, the results indicate that the intracellular

target of FITC-RHAU18 is most likely G4s and primarily are mtDNA G4s.

To confirm the selectivity of FITC-RHAU18 targeting G4s in cells, Cy5-tagged mt10252 (parallel G4), mt714 (antiparallel G4), mt1015 (hybrid G4), and HP19 (dsDNA) were transfected into Huh7 cells to study the intracellular interactions between FITC-RHAU18 and these Cy5-tagged substrates. We observed that the transfected mt10252 co-localized well with FITC-RHAU18 in cells, with a Pearson's coefficient of 0.663. Moreover, for the other three nucleic acid substrates, which were not parallel-type G-quadruplexes, showed minimal co-localization (Figure 3b) and the Pearson's coefficient was less than 0.33. These results indicate that FITC-RHAU18 may selectively bind to parallel-type G4-mtDNA in living cells.

Additionally, we evaluated the difference of FITC-RHAU18 in imaging normal and cancer cells. Using various concentrations of FITC-RHAU18 to stain and image a variety of live cells for 2 hours, a significant increase in the number of green fluorescent foci was observed with an increase of FITC-RHAU18 concentration in Huh7, mouse colon carcinoma (MC38), and human non-small cell lung cancer (H1975) cells. In contrast, normal cells such as human embryonic kidney cells (293T), human immortalized epidermal cells (HaCaT), and human mammary cells (HBL100) showed no such obvious fluorescent foci observed until the concentration of FITC-RHAU18 was increased to 20 μM (Figure 4). These results indicate that the parallel G4-mtDNA is significantly enriched in cancer cells than in normal cells, paving the way for the development of a highly specific and sensitive ^{18}F-radiolabeled probe targeting mtDNA for the visualization and imaging of cancer cells with PET. The features of FITC-RHAU18 demonstrated strongly support the feasibility for the incorporation of fluorine-18 into RHAU18 for PET imaging of G4-mtDNA *in vivo*.

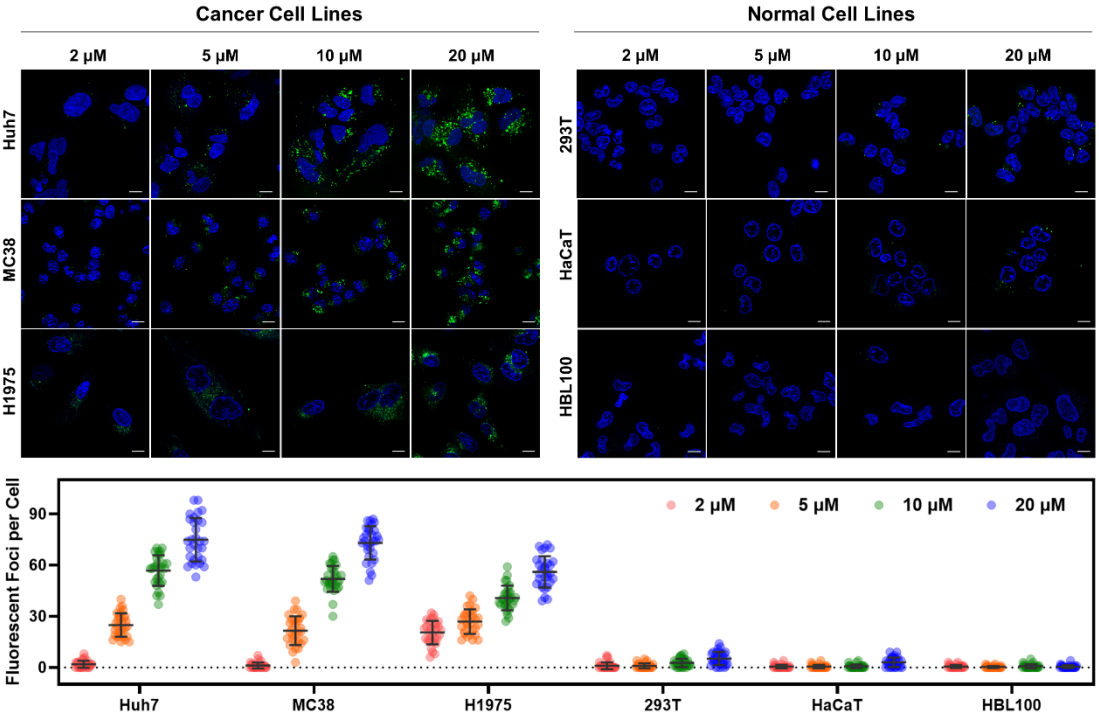

Figure 4. Live cancer cells and normal cells were stained with 10 μM FITC-RHAU18 at different concentrations for 2 h and 1 μM Hoechst33342 for 15 min. For each sample of cell image, 30 cells were measured. The data are presented as mean ± SEM. Scale bars for cell image: 10 μm.

The *in vivo* micro-PET imaging and pharmacokinetic analysis. Considering the favorable specificity and performance of FITC-RHAU18 targeting G4-mtDNA in living cancer cells, we further sought to develop peptide probe [^{18}F]AlF-NOTA-RHAU18 for live animal study. The tracer was synthesized using the [^{18}F]AlF-NOTA approach with a radiochemical yield of 19.5 ± 3.9%, a radiochemical purity of over 99%, and a specific activity of 14.9 ± 3.3 GBq/μmol. The significant uptake of [^{18}F]AlF-NOTA-RHAU18 and an internalization rate of about 45% were observed experimentally in tumor cells (Supplementary Figures S9 and S10). This behavior was an unexpected finding and the delivery mechanism has not been elucidated. We speculate that it could be mediated by positive-charged character of the probe or uptake through membrane bilayer transport and endocytosis.

Dynamic micro-PET imaging was conducted on Huh7 tumor-bearing mice to investigate the real-time biodistribution of [^{18}F]AlF-NOTA-RHAU18. Representative coronal images and time-activity curves demonstrated the uptake of [^{18}F]AlF-NOTA-RHAU18 in Huh7 tumors and

revealed its *in vivo* pharmacokinetics in vital organs of the mice (Figure 5a and 5b). The probe was cleared primarily in kidney and liver. Specific uptake of [^{18}F]AlF-NOTA-RHAU18 in Huh7 tumors was observed, with tumor-to-muscle (T/M) ratios increasing over time (Supplementary Figure S11).

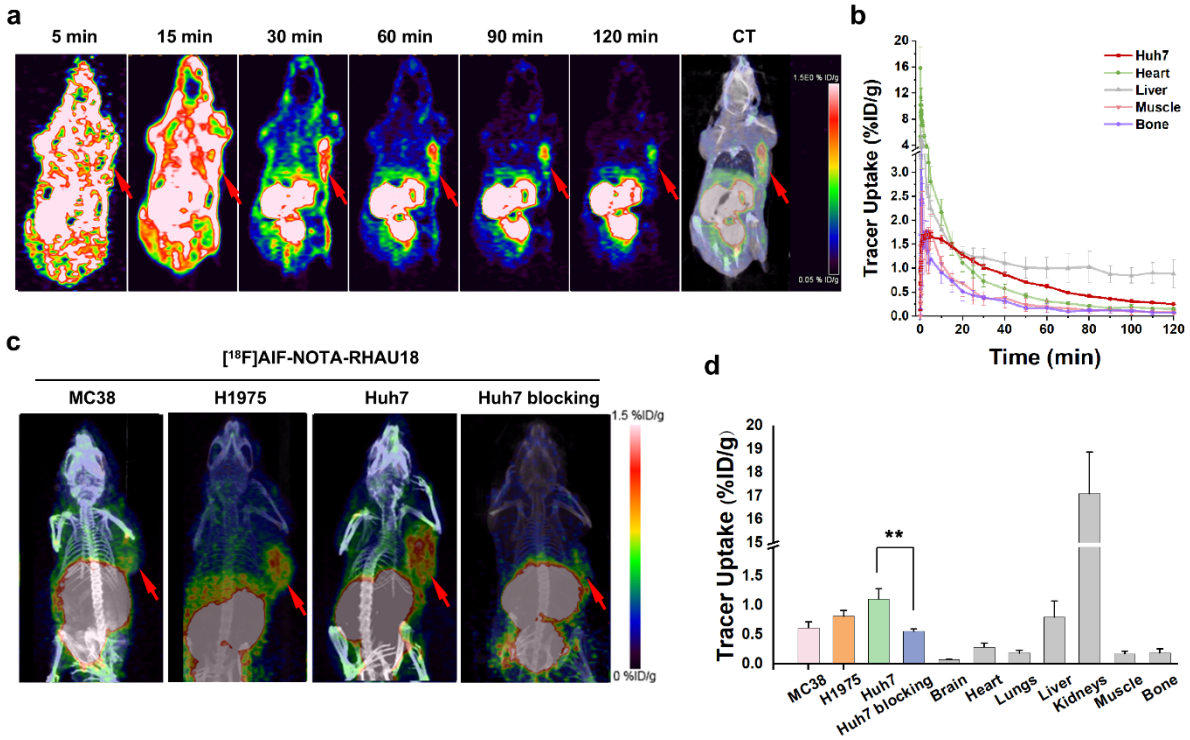

Figure 5. (a) *In vivo* dynamic micro-PET scan imaging of [^{18}F]AlF-NOTA-RHAU18 in male BALB/c-nu mice bearing Huh7 tumor. Arrows indicate location of tumors. (b) Time-activity curves of major organs and tumors after intravenous injection of [^{18}F]AlF-NOTA-RHAU18. (c) Whole body MIP/CT images of [^{18}F]AlF-NOTA-RHAU18 in nude mice bearing MC38, H1975, and Huh7 (uptake and blocking) tumors at 1 h after intravenous injection. (d) Quantitative analysis of [^{18}F]AlF-NOTA-RHAU18 static uptake and inhibition in major organs at 60 min. Biological replicates (n = 3) were taken.

Static Micro-PET imaging studies were performed on Huh7, H1975 and MC38 tumor models. Representative maximum intensity projection/Computed Tomography (MIP/CT) images containing different tumor-bearing mice at 1 h post injection was shown in Figure 5c. The signal of [^{18}F]AlF-NOTA-RHAU18 was clearly observed in different tumors, indicating its ability as a broad-spectrum PET tracer[30]. Tissue uptake (percentage of injected dose per gram of tissue, %ID/g) in MC38, H1975 and Huh7 were 0.62 ± 0.11 %ID/g, 0.82 ± 0.09 %ID/g,

and 1.11 ± 0.18 %ID/g, respectively. Huh7 had the highest tumor-to-muscle ratio, which was 6.72 ± 0.98. The tumor-specificity of [^{18}F]AlF-NOTA-RHAU18 probe shown in Figure 5c was confirmed on the basis of blocking in Huh7 (0.56 ± 0.04 %ID/g, P = 0.0079). The biodistribution of [^{18}F]AlF-NOTA-RHAU18 in Huh7 tumor-bearing nude mice at 60 min p.i. was basically consistent with static imaging data (Supplementary Figure S11 and Figure 5d). It is noteworthy that only picomolar concentration of the tracer is required to provide high-resolution imaging, which is a significantly lower concentration compared to the traditional fluorescent probes. Therefore, the radioactive PET peptide probe not only offers high resolution and high tissue penetration, but also provides advantages in terms of drug safety and metabolism.

The biodistribution value of Huh7 tumor was 0.77 ± 0.14 %ID/g, which was generally consistent with static imaging data. Signal enrichment in the liver and kidney may reflect clearance of the probe through these organs (Supplementary Figure S12). We have also shown that [^{19}F]AlF-NOTA-RHAU18 has no toxic effects on normal liver and kidney cells (Supplementary Figure S13).

To further investigate the *in vivo* pharmacokinetic property of [^{18}F]AlF-NOTA-RHAU18, we selected the time activity curve of major artery as the whole blood input function to conduct kinetic modeling and graphical analysis for uptake in a Huh7 tumor model (Figure 6a)[31]. Time-activity curve analysis of Huh7 tumors showed that tumor uptake was peaked at 4 minutes and then declined over time, which was consistent with reversible pharmacokinetic properties. The graphical models of logan and patlak were then analyzed. The results also showed a good fit between tumor uptake and the reversible logan model (R^2 = 0.983, Figure 6b and 6c). We performed a comparison of the fitting results between the one-tissue-compartment (1TCM), the reversible two-tissue compartment (re-2TCM) and the irreversible two-tissue compartment (irre-2TCM) model. The Akaike Information Criterion (AIC)[32] value of re-2TCM was lower than those of 1TCM and irre-2TCM. In addition, the distribution volume (V_D) value of re-2TCM (1.4202) is closer to the logan graphical model (1.3196) (Figure 6d). This observation suggests that the metabolism of [^{18}F]AlF-NOTA-RHAU18 is more consistent with the reversible two-tissue compartment model.

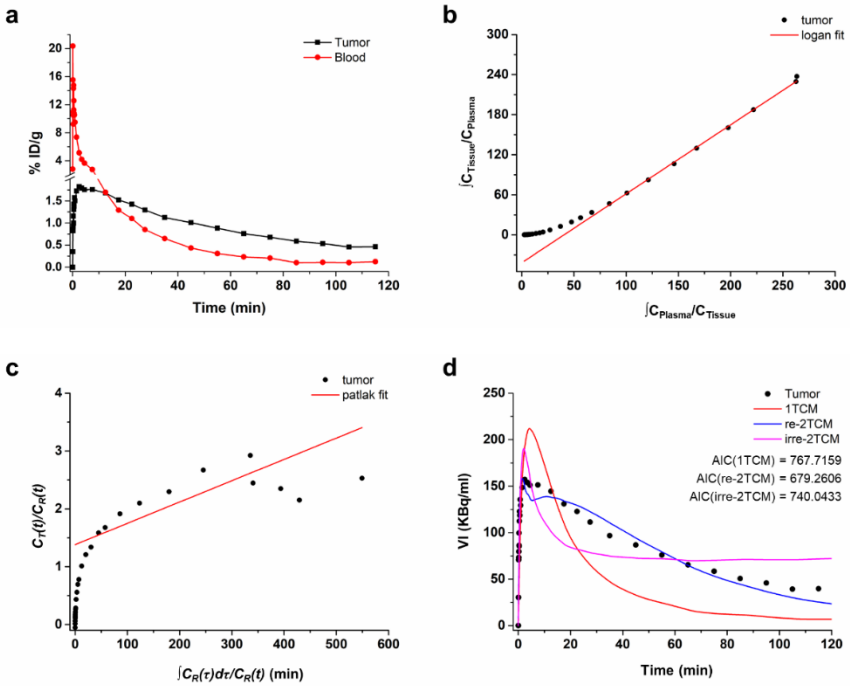

Figure 6. (a) Representative time-activity curves of blood and Huh7 tumor uptakes of [^{18}F]AlF-NOTA-RHAU18 in Huh7 tumor-bearing mice. (b) Logan graphical analysis of representative tumor TAC for Huh7 models. (c) Patlak graphical analysis of representative tumor TAC for Huh7 models. (d) One-tissue-compartment reversible model fitting, reversible two-tissue compartment (re-2TCM) model fitting and irreversible two-tissue compartment (irre-2TCM) of the same representative TAC.

CONCLUSIONS

In conclusion, we reported a PET peptide probe, [^{18}F]AlF-NOTA-RHAU18, derived from the DEAH box deconjugating enzyme RHAU. This is the first *in vivo* detection of G4s using radionuclide fluorine-18, with a high selectivity targeting mitochondrial parallel G4-DNAs. In the study, we discovered that more abundant parallel mitochondrial G4s was found in cancer cells compared to normal cells. The specificity and affinity of this peptide probe targeting G4s were validated both *in vitro* and *in vivo*. The signal enrichment of the probe was also successfully observed in tumors of homozygous mice. This peptide probe overcomes the limitations of traditional fluorescent small-molecule G4-ligands because the use of radionuclide fluorine-18 can image deeper tissues and organs. Combined with PET/CT technology, the probe also enables more precise localization of *in vivo* target at the tumor site. Additionally, this peptide probe is highly sensitive, down to pM level, and can be rapidly cleared from the bloodstream. It is essentially free of drug toxicity. Therefore, this G4-targeting

peptide probe shows great potential to develop as a sensitive cancer diagnostic tool.

EXPERIMENTAL SECTION

Materials. The oligonucleotide used in the experiments are listed in Supplementary Table S1 and S2. All oligonucleotide used in the present study were purchased from IGE Bio and the sequences were shown in Table S1 and S2. All oligonucleotides were adjusted to 200 μM with phosphate buffer, heated in a water bath and held at 95 °C for 15 min, then slowly cooled to room temperature and incubated at 4 °C overnight. Before use, the samples were diluted with the same buffer to the working concentration. RHAU18, NOTA-RHAU18 and FITC-RHAU18 were all purchased from HongTide Biotech with a purity of over 98%.

Radiolabeling. NOTA-RHAU18 was dissolved in a 10 mL glass vial with 350 μL dimethyl sulfoxide(DMSO) and 16 μL of 2 mM $AlCl_3$ in 0.2 M NaOAC solution(PH = 4.0). Around 3700 MBq fluorine-18 were passed through a preconditioned QMA cartridge. Purified fluorine-18 was eluted with 450 μL of 0.5 M sodium acetate buffer (pH = 3.9 - 4.0) from the QMA cartridge and added into the glass vial. The mixture was heated at 110 °C for 15-20 min after vortexing carefully. The reaction liquid was diluted with 8 mL cold water and purified on a C18 cartridge with 40 mL water and 10 mL air. [^{18}F]AlF-NOTA-RHAU18 was eluted with 600 μL of 10 mM hydrochloric acid ethanol (10 mM HCl in pure ethanol) and diluted with 6 mL 0.9% saline before injection.

Radiochemical purity determination. Radiochemical purity was determined by high performance liquid chromatography (HPLC) on a Kromasil 100-5 column (C18, 4.6 × 250 mm, 5 μ) with an SPD-M20A full wavelength UV detector and a Bioscan radioactivity detector. The mobile phase was composed of two different solutions. Solution A was pure water with 0.1 % trifluoroacetic acid (TFA). Solution B was pure acetonitrile with 0.1 % TFA. The flow rate was set to 1 mL/min. The concentration of phase B started at 5 % and increased to 45 % at 2 min, 90 % at 9 min, and 5 % at 12 min. The column was first cleaned with methanol, and after a stable baseline was observed after about 20 min, the column was further equilibrated with an experimental solution of appropriate flow for another 20 min, and after the baseline was again stable, auto-sampling was performed under the same conditions for the acquisition of the ^{19}F-NOTA-RHAU18 standard solution and the [^{18}F]AlF-NOTA-RHAU18solution to be tested. The

collected data were then analyzed using HPLC software to obtain UV absorption spectra and radioactivity maps, and the radiochemical purity of the [^{18}F]AlF-NOTA-RHAU18 compound was found to be > 99%.

Partition coefficient study. 300 MBq [^{18}F]AlF-NOTA-RHAU18, 5 mL phosphate-buffered saline (PBS) (pH = 7.4), and 5 mL octanol were added into a 15 mL centrifuge tube. The solution was vortexed and centrifuged (1000rpm, 5min) at room temperature. 500 μL solution of different layers were counted with a γ-Counter (CAPRAC-R, Capintec, Inc., Ramsey, NJ, USA) and logP values were calculated (n = 4).

In vitro and in vivo stability. The *in vitro* stability of [^{18}F]AlF-NOTA-RHAU18 was investigated in PBS buffer and FBS. 14.8-18.5 MBq of [^{18}F]AlF-NOTA-RHAU18 was added into the vial with 200 μL FBS or PBS buffer and vortexed gently. After cultivating at room temperature for 2 h, the mixture was analyzed by a HPLC with radioactivity detector (BIOSCAN, USA). The in vivo stability of [^{18}F]AlF-NOTA-RHAU18 was inspected in blood and urine of tumor-bearing mice. 11.1-18.5 MBq of [^{18}F]AlF-NOTA-RHAU18 was injected through the tail vein. The blood from eyeballs and urine were extracted 1h after injection. The filtered blood and urine were counted in γ-Counter and HPLC separately after filtered. *In vitro* and *in vivo* stability experiments were performed using the same batch of synthesized radiolabeled compounds, and each set of experiments was repeated three times .

Isothermal titrimetric calorimetry. The experiments were carried out in a MicroCal PEAQ-ITC (Malvern, USA) microcalorimeter. Oligonucleotides were pre-annealed in 25 mM KH_2PO_4, 60 mM KCl buffer (pH 7.4) by heated to 95 °C in water bath for 10 min. Then, it was cooled to 25 °C and placed at 4 °C overnight. Annealed oligonucleotides (200 μM) in buffer were filled in the syringe and the peptides (10 μM) in the same buffer were kept in the sample cell. Oligonucleotides were then mixed with the peptide solution under the specific conditions of 750 rpm, 25°C, and the ligand was injected into the cuvette in a total of 19 or 25 drops, with a duration of 4 seconds per drop and an interval of 150 seconds between shots. Finally, kinetic and thermodynamic parameters of nucleic acids and peptides were obtained by fitting the data to appropriate computational models.

Electrophoretic mobility shift assay. Oligonucleotides were incubated at 37°C for 3 hours with or without the addition of peptides, and then the samples were loaded on a 20%

polyacrylamide-bisacrylamide (29:1) gel at a final concentration of 5 μM for nucleic acids and 100 μM for peptides. Electrophoresis experiments were carried out in 0.5× TBE buffer at 4°C under the following conditions: run at 60 V for 30 minutes and then at 110 V for 90 minutes. At the end of electrophoresis, the gel was stained with 5 μM SYBR Gold to avoid light, followed by imaging on an AlphaImager HP automated gel imager.

Circular dichroism spectroscopy. CD studies were performed on a Chirascan spectrophotometer (Applied Photophysics). The spectra data was collected from 195 nm to 260 nm with a bandwidth of 1 nm, a 1 step of 1 nm, and a scanning time of 0.5 sec/point. The data were averaged over three scans and the CD spectra were then analyzed using CDNN software to elucidate the relative amounts of specific secondary structures of the peptides.CD melting measurement was set as a fixed wavelength, while gradually increasing the temperature from 20 to 95 °C at a heating rate of 1 °C /min. Data plotting and analysis with Origin and GraphPad Prism.

Cell lines and cell cultures. Huh7, H1975, MC38, 293T, HaCaT and HBL100 cells were obtained from the Institute of Biochemistry and Cell Biology, Shanghai Institutes for Biological Sciences (Shanghai, China). Huh7, MC38, 293T, HaCaT and HBL100 cells were cultivated in DMEM with 10% FBS and 1% Penicillin-Streptomycin solution and incubated in 37 °C in an atmosphere with 5% CO_2. H1975 and LO2 cells were cultivated in RPMI 1640 with 10 % FBS and 1% Penicillin-Streptomycin solution and incubated in 37 °C in an atmosphere with 5% CO_2. For the preparation of ρ0 Huh7 cells, parental Huh7 cells were cultured for 30−40 days in low-dose EtBr (Sigma) (50 ng/mL) supplemented with 1 mM pyruvate (Sigma) and 50 mg/mL uridine (Sigma) followed by transfer to medium lacking EtBr. For the preparation of exogenous nucleic acid-transfected Huh7 cells, treated Cy5 DNA was introduced into Huh7 cells with Lipofectamine 3000 and then incubated for 24 hours at 37 °C and 5% CO_2 in an incubator.

Live cell imaging. Cells were seeded in a glass-bottomed 96-well plate (Thermo Fisher Scientific) at 5,000 cells per well and grew overnight. MitoTracker Deep Red (Invitrogen, M22426) were used to indicate mitochondria, and Hoechst33342 (Thermo Fisher Scientific, #62249) was used to indicate nucleus. For cyclosporin (CsA) treatment, cells were treated with 1 μM CsA for 24 h to block the permeability transition pore on the inner membrane of

mitochondria. After CsA treatment, the cells were washed with DMEM and then stained with 10 μM FITC-RHAU18 for 2 h. For FCCP treatment, cells were treated with 1 μM FCCP for 30 min to depolarize the cells. After FCCP treatment, the cells were washed with DMEM and then stained with 10 μM FITC-RHAU18 for 2 h. For G-quadruplex ligand competition assays, cells were first treated overnight with 5 μM or 10 μM MitoPDS or BRACO19 respectively, the medium was washed away and the cells were then stained with 10 μM FITC-RHAU18 for 2 h. For staining experiments on different cell lines, cells were seeded in a glass-bottomed 96-well plates at 5,000 cells per well and incubated in an incubator at 37 °C and 5% CO_2 for 24 h, then cells were stained with 10 μM FITC-RHAU18 for 2 h. Samples were finally imaged on a Carl Zeiss LSM 800 super high-resolution laser confocal microscope. The images were analyzed with Imaris software (Bitplane Corp.). For Hoechst33342 imaging, the laser wavelength was 405 nm and the detection wavelength was 400-480nm. For FITC-RHAU18 imaging, the laser wavelength was 488nm and the detection wavelength was 505-550nm. For MitoTracker imaging, the laser wavelength was 561 nm and the detection wavelength was 600-650 nm. For Cy5-labelled DNA imaging, the laser wavelength is 640 nm and the detection wavelength is 650-700 nm.

Fixed cell imaging. Huh7 cells were seeded in a glass-bottomed 96-well plate (Thermo Fisher Scientific) at 5,000 cells per well and grew overnight. The samples were fixed with 4% paraformaldehyde in PBS at 4 °C for 15 min and permeabilized with 0.5% Triton X-100 in PBS at 37 °C for 20 min. For enzyme-digestion experiments, cells were incubated with 200 units·mL^{-1} RNase A (Thermo Fisher Scientific, EN0531) or DNase I (Thermo Fisher Scientific, EN0523) at 37 °C for 5 hours after permeabilization. Subsequently, they were stained with 5 μM FITC-RHAU18 for 30 min. For ligand replacement experiments, cells were initially stained with 5 μM FITC-RHAU18 for 30 min. The medium was then washed away, and the cells were treated with 2 μM, 5 μM, and 10 μM of the G-quadruplex ligand BRACO19 for 2 h, respectively. Samples were finally imaged on a Carl Zeiss LSM 800 super high resolution laser confocal microscope. The images were analyzed with Imaris software (Bitplane Corp.). For Hoechst33342 imaging, the laser wavelength was 405 nm and the detection wavelength was 400-480nm. For FITC-RHAU18 imaging, the laser wavelength was 488nm and the detection wavelength was 505-550nm.

Cytotoxicity test. 293T and LO2 cells were seeded in 96-well plate at 5000 cells per well and grew overnight. Complete medium containing different gradient [^{19}F]AlF-NOTA-RHAU18 was added. The culture was continued at 37 °C and 5% CO2 for 12 h. After removal of the medium from the 96-well plate, 100 μL of 10% CCK8 solution was added to each well and then the 96-well plate was kept away from light for 2 h. The 96-well plate was transferred to the Microplate reader, and its absorbance was measured at 450 nm. Finally, the cell survival rate was determined according to the absorbance value.

Cellular uptake experiment. For the cell uptake studies, Huh7 cells and 293T cells were seeded into 24 well plates and cultured for 24 h until reaching a final confluence of over 90 %. The medium was removed, and the cells were washed with PBS. Subsequently, the cells were incubated with 0.5 mL of serum-free medium containing [^{18}F]AlF-NOTA-RHAU18 (111 kBq) for 15, 30, 60, 90 and 120 min at 37 °C. Following the incubation period, cells were washed twice with PBS and lysed with NaOH-SDS (sodium dodecyl sulfate, 0.2 M NaOH, 1 % SDS). Finally, cellular lysates were collected and measured using gamma counter. For the cell blocking experiments, Huh7 cells were co-incubated the [^{18}F]AlF-NOTA-RHAU18 and 2 μg of RHAU18 for 120 min.

Cellular internalization experiment. The internalization experiments were performed by incubating the Huh7 cells with [^{18}F]AlF-NOTA-RHAU18 for 120 min. Then, the cells were washed twice with PBS and incubated with 1 mL glycine of HCl (1 M, pH 2.2) for 10 min to detach the extracellular bound tracer. Next, the cells were washed twice with PBS and were then lysed with NaOH-SDS. The radioactivity of the acid wash solution (extracellularly bound tracer) and cell lysate (internalized tracer) was detected separately using a gamma counter.

Xenograft tumor model. Animal studies were performed under Nangfang Hospital Animal Ethics Committee (ACUC-approved protocol, protocol number IACUC-LAC-20220920-003). 2×10^5 cells were implanted subcutaneously at right flank of 5-week-old male BALB/cNj-Fpxn1^{nu}/Gpt mice(GemPharmatech Co., Ltd). The tumor-bearing mice were fed at specific pathogen-free(SPF) environment with ample food and water. The tumor models were available when the tumor diameter reached 6-15 millimeters.

Tissue biodistribution studies. Tumor xenografts mice were fasted for 6 h and

euthanized after 1h injection of [^{18}F]AlF-NOTA-RHAU18 (1.11-1.46 MBq/mouse, n = 4). The blood, organs and tumor were removed and weighted. The collected samples were counted via a γ-Counter. The CPM value of samples were transferred into the percentage of injected dose per gram (%ID/g).

Micro-PET imaging and pharmacokinetic analysis. Dynamic micro-PET imaging was performed on the tumor-bearing mice (7.4 MBq/mouse, n = 4). The anaesthetized mice were place into the small animal PET scanner, via an Inveon Micro-PET/CT scanner (Siemens, Erlangen, Germany). The 2 h dynamic micro-PET scan and the injection of [^{18}F]AlF-NOTA-RHAU18 were started simultaneously. The uptake static imaging was performed 1 h after the injection of [^{18}F]AlF-NOTA-RHAU18 on different tumor-bearing mice. For blocking experiment, the [^{18}F]AlF-NOTA-RHAU18(7.4 MBq/mouse) and RHAU18 (250 μg/mouse) were coinjected into Huh-7 mice intravenously. Static micro-PET scan was performed 1 h after injection. The images were reconstructed with the OSME3D/SP-MAP algorithm (OSEM Iterations was 2, MAP Iterations was 18, and Target resolution was 1.5 mm) and the Matrix size setting was 256×256. Attenuation correction is performed with a low dose CT called CTAC (The CT reconstruction parameters were as follows: Algorithm was Feldkamp, Noise Reduction was slight, Filter was shepp-logan, Apply HU scaling factor was 3.244). The tissue uptake was analyzed by the regions of interest (ROIs) drawn over the tumor and interest organs. For PET/CT image processing, the color bar was set to 0 or 0.05 to 1.5 %ID/g (percentage of injected dose per gram of tissue) for PET images, -1000 to 550 HU for CT images, and 400 to 2800 HU for MIP images. The pharmacokinetic analysis was performed in PMOD and IRW software. First, TACs of the major artery and Huh7 tumor were delineated by IRW, and quantitative data were derived. Then, the TAC of the major artery as the blood pool input function and different pharmacokinetic models were selected for simulation analysis. For comparative analysis, we selected and analyzed the one-tissue compartment (1TCM), reversible two-tissue compartment (re-2TCM), irreversible two-tissue compartment (irre-2TCM), and two graphical models: logan and patlak. An adequate compartment model was chosen based on the Akaike information criterion (AIC) and the correlation coefficient.

ASSOCIATED CONTENT

Supporting Information. All data are available in the main text or the supplementary materials.

AUTHOR INFORMATION

Corresponding Authors

Yu-Jing Lu – *Guangdong Medicine-Engineering Interdisciplinary Technology Research Center, School of Biomedical and Pharmaceutical Sciences, Guangdong University of Technology, Guangzhou 510006, China*

Smart Medical Innovation Technology Center, Guangdong University of Technology, Guangzhou 510006, China

Shun Huang – *Department of Nuclear Medicine, The Tenth Affiliated Hospital, Southern Medical University (Dongguan People's Hospital), Dongguan 523059, China*

Authors

Xiao-Chun Guo – *School of Biomedical and Pharmaceutical Sciences, Guangdong University of Technology, Guangzhou 510006, China*

Da-Zhi Shi – *Department of Nuclear Medicine, Nanfang Hospital, Southern Medical University, guangzhou 510515, China*

Yi-Han Zhang – *School of Biomedical and Pharmaceutical Sciences, Guangdong University of Technology, Guangzhou 510006, China*

Wan-Ying Zhang – *School of Biomedical and Pharmaceutical Sciences, Guangdong University of Technology, Guangzhou 510006, China*

Jing Chen – *School of Biomedical and Pharmaceutical Sciences, Guangdong University of Technology, Guangzhou 510006, China*

Zebin Huang – *School of Biomedical and Pharmaceutical Sciences, Guangdong University of Technology, Guangzhou 510006, China*

Hubing Wu – *Department of Nuclear Medicine, Nanfang Hospital, Southern Medical University, Guangzhou 510515, China*

Jinqiang Hou – *Department of Chemistry, Lakehead University, 955 Oliver Road, Thunder*

Bay, Ontario P7B 5E1, Canada

Thunder Bay Regional Health Research Institute, 980 Oliver Road, Thunder Bay, Ontario P7B 6V4, Canada

Fu-Jun Jin – *School of Biomedical and Pharmaceutical Sciences, Guangdong University of Technology, Guangzhou 510006, China*

Xiu-Cai Chen – *School of Biomedical and Pharmaceutical Sciences, Guangdong University of Technology, Guangzhou 510006, China*

Wing-Leung Wong – *State Key Laboratory of Chemical Biology and Drug Discovery, Department of Applied Biology and Chemical Technology, The Hong Kong Polytechnic University, Hung Hom, Kowloon, Hong Kong SAR 999077, China*

Author Contributions

X. G. carried out in vitro validation experiments and visualisation experiments in cells. D.S. carried out the radiochemistry experiments and visualisation experiments in animals. Y. L. and S. H. convinced the idea and supervised the work. All authors discussed the results and contributed to the manuscript.

Funding

This work was supported by the National Natural Science Foundation of China (No. 22077020), the Natural Science Foundation of Guangdong Province (No. 2023A1515011952), the Guangdong Basic and Applied Basic Research Foundation (Nos. 2022A1515140033 and 2024A1515010769), The Overseas Famous Teachers Project of Guangdong Provincial Department of Science and Technology(No. GK4220026), the Smart Medical Innovation Technology Center, GDUT (No. ZYZX24-041), and the Doctoral Initiation Project of The Tenth Affiliated Hospital of Southern Medical University (Dongguan People's Hospital) (No. K202410).

ACKNOWLEDGMENTS

We would like to thank Dr. Xiao Zhou and Dr. Hang Bai from the Analysis and Test Center, Guangdong University of Technology for their assistance in cell imaging experiments. We also

acknowledged Dr. Jia-Heng Tan, Professor of Sun Yat-sen University, for providing us the compound MitoPDS.

Notes

The authors have no conflicts of interest to declare.

REFERENCES

(1) Sen, D.; Gilbert, W. Formation of parallel four-stranded complexes by guanine-rich motifs in DNA and its implications for meiosis. *Nature* **1988**, *334* (6180), 364-366. DOI: 10.1038/334364a0. Kwok, C. K.; Marsico, G.; Sahakyan, A. B.; Chambers, V. S.; Balasubramanian, S. rG4-seq reveals widespread formation of G-quadruplex structures in the human transcriptome. *Nat Methods* **2016**, *13* (10), 841-844. DOI: 10.1038/nmeth.3965.

(2) Yang, D. Z.; Okamoto, K. Structural insights into G-quadruplexes: towards new anticancer drugs. *Future Med Chem* **2010**, *2* (4), 619-646. DOI: 10.4155/Fmc.09.172. Zhang, S. L.; Wu, Y. L.; Zhang, W. G-Quadruplex Structures and Their Interaction Diversity with Ligands. *Chemmedchem* **2014**, *9* (5), 899-911. DOI: 10.1002/cmdc.201300566.

(3) Hänsel-Hertsch, R.; Simeone, A.; Shea, A.; Hui, W. W. I.; Zyner, K. G.; Marsico, G.; Rueda, O. M.; Bruna, A.; Martin, A.; Zhang, X. Y.; et al. Landscape of G-quadruplex DNA structural regions in breast cancer. *Nat Genet* **2020**, *52* (9), 878-883. DOI: 10.1038/s41588-020-0672-8.

(4) Chambers, V. S.; Marsico, G.; Boutell, J. M.; Di Antonio, M.; Smith, G. P.; Balasubramanian, S. High-throughput sequencing of DNA G-quadruplex structures in the human genome. *Nat Biotechnol* **2015**, *33* (8), 877-881. DOI: 10.1038/nbt.3295. Bhattacharyya, D.; Arachchilage, G. M.; Basu, S. Metal Cations in G-Quadruplex Folding and Stability. *Front Chem* **2016**, *4*, 38. DOI: ARTN 38
10.3389/fchem.2016.00038.

(5) Neidle, S. Human telomeric G-quadruplex: The current status of telomeric G-quadruplexes as therapeutic targets in human cancer. *Febs J* **2010**, *277* (5), 1118-1125. DOI: 10.1111/j.1742-4658.2009.07463.x. Merle, P.; Gueugneau, M.; Teulade-Fichou, M. P.; Müller-Barthélémy, M.; Amiard, S.; Chautard, E.; Guetta, C.; Dedieu, V.; Communal, Y.; Mergny, J. L.; et al. Highly efficient radiosensitization of human glioblastoma and lung cancer cells by a G-quadruplex

DNA binding compound. *Sci Rep-Uk* **2015**, *5*, 16255. DOI: ARTN 16255 10.1038/srep16255. Varshney, D.; Spiegel, J.; Zyner, K.; Tannahill, D.; Balasubramanian, S. The regulation and functions of DNA and RNA G-quadruplexes. *Nat Rev Mol Cell Bio* **2020**, *21* (8), 459-474. DOI: 10.1038/s41580-020-0236-x.

(6) Han, H. Y.; Hurley, L. H. G-quadruplex DNA: a potential target for anti-cancer drug design. *Trends Pharmacol Sci* **2000**, *21* (4), 136-142. DOI: Doi 10.1016/S0165-6147(00)01457-7. Kosiol, N.; Juranek, S.; Brossart, P.; Heine, A.; Paeschke, K. G-quadruplexes: a promising target for cancer therapy. *Mol Cancer* **2021**, *20* (1), 40. DOI: ARTN 40 10.1186/s12943-021-01328-4. Neidle, S. Quadruplex nucleic acids as targets for anticancer therapeutics. *Nat Rev Chem* **2017**, *1* (5), 0041. DOI: ARTN 0041 10.1038/s41570-017-0041.

(7) Di Antonio, M.; Ponjavic, A.; Radzevicius, A.; Ranasinghe, R. T.; Catalano, M.; Zhang, X. Y.; Shen, J. Z.; Needham, L. M.; Lee, S. F.; Klenerman, D.; et al. Single-molecule visualization of DNA G-quadruplex formation in live cells. *Nat Chem* **2020**, *12* (9), 832-837. DOI: 10.1038/s41557-020-0506-4.

(8) Biffi, G.; Tannahill, D.; McCafferty, J.; Balasubramanian, S. Quantitative visualization of DNA G-quadruplex structures in human cells. *Nat Chem* **2013**, *5* (3), 182-186. DOI: 10.1038/Nchem.1548.

(9) Chen, X. C.; Chen, S. B.; Dai, J.; Yuan, J. H.; Ou, T. M.; Huang, Z. S.; Tan, J. H. Tracking the Dynamic Folding and Unfolding of RNA G-Quadruplexes in Live Cells. *Angew Chem Int Edit* **2018**, *57* (17), 4702-4706. DOI: 10.1002/anie.201801999.

(10) Zheng, K. W.; Zhang, J. Y.; He, Y. D.; Gong, J. Y.; Wen, C. J.; Chen, J. N.; Hao, Y. H.; Zhao, Y.; Tan, Z. Detection of genomic G-quadruplexes in living cells using a small artificial protein. *Nucleic Acids Res* **2020**, *48* (20), 11706-11720. DOI: 10.1093/nar/gkaa841.

(11) Yan, J. W.; Chen, S. B.; Liu, H. Y.; Ye, W. J.; Ou, T. M.; Tan, J. H.; Li, D.; Gu, L. Q.; Huang, Z. S. Development of a new colorimetric and red-emitting fluorescent dual probe for G-quadruplex nucleic acids. *Chem Commun* **2014**, *50* (52), 6927-6930. DOI: 10.1039/c4cc01472c.

(12) Chen, X. C.; Tang, G. X.; Luo, W. H.; Shao, W.; Dai, J.; Zeng, S. T.; Huang, Z. S.; Chen, S. B.; Tan, J. H. Monitoring and Modulating mtDNA G-Quadruplex Dynamics Reveal Its Close

Relationship to Cell Glycolysis. *J Am Chem Soc* **2021**, *143* (49), 20779-20791. DOI: 10.1021/jacs.1c08860.

(13) Chang, C. C.; Kuo, I. C.; Lin, J. J.; Lu, Y. C.; Chen, C. T.; Back, H. T.; Lou, P. J.; Chang, T. C. A novel carbazole derivative, BMVC: A potential antitumor agent and fluorescence marker of cancer cells. *Chem Biodivers* **2004**, *1* (9), 1377-1384. DOI: DOI 10.1002/cbdv.200490100.

(14) Feng, Y.; Yang, D. Z.; Chen, H. B.; Cheng, W. L.; Wang, L. X.; Sun, H. X.; Tang, Y. L. Stabilization of G-quadruplex DNA and inhibition of Bcl-2 expression by a pyridostatin analog. *Bioorg Med Chem Lett* **2016**, *26* (7), 1660-1663. DOI: 10.1016/j.bmcl.2016.02.065.

(15) Yang, Q. F.; Xiang, J. F.; Yang, S.; Li, Q.; Zhou, Q. J.; Guan, A. J.; Zhang, X. F.; Zhang, H.; Tang, Y. L.; Xu, G. Z. Verification of specific G-quadruplex structure by using a novel cyanine dye supramolecular assembly: II. The binding characterization with specific intramolecular G-quadruplex and the recognizing mechanism. *Nucleic Acids Res* **2010**, *38* (3), 1022-1033. DOI: 10.1093/nar/gkp1045.

(16) Henderson, A.; Wu, Y. L.; Huang, Y. C.; Chavez, E. A.; Platt, J.; Johnson, F. B.; Brosh, R. M.; Sen, D.; Lansdorp, P. M. Detection of G-quadruplex DNA in mammalian cells. *Nucleic Acids Res* **2014**, *42* (2), 860-869. DOI: 10.1093/nar/gkt957.

(17) Sharma, T.; Kundu, N.; Kaur, S.; Shankaraswamy, J.; Saxena, S. Why to target G-quadruplexes using peptides: Next-generation G4-interacting ligands. *J Pept Sci* **2023**, *29* (10), 3491. DOI: 10.1002/psc.3491.

(18) Lattmann, S.; Giri, B.; Vaughn, J. P.; Akman, S. A.; Nagamine, Y. Role of the amino terminal RHAU-specific motif in the recognition and resolution of guanine quadruplex-RNA by the DEAH-box RNA helicase RHAU. *Nucleic Acids Res* **2010**, *38* (18), 6219-6233. DOI: 10.1093/nar/gkq372.

(19) Heddi, B.; Cheong, V. V.; Martadinata, H.; Phan, A. T. Insights into G-quadruplex specific recognition by the DEAH-box helicase RHAU: Solution structure of a peptide-quadruplex complex. *P Natl Acad Sci USA* **2015**, *112* (31), 9608-9613. DOI: 10.1073/pnas.1422605112. Meier, M.; Patel, T. R.; Booy, E. P.; Marushchak, O.; Okun, N.; Deo, S.; Howard, R.; McEleney, K.; Harding, S. E.; Stetefeld, J.; et al. Binding of G-quadruplexes to the N-terminal Recognition Domain of the RNA Helicase Associated with AU-rich Element (RHAU). *J Biol Chem* **2013**,

288 (49), 35014-35027. DOI: 10.1074/jbc.M113.512970. Roy, S.; Ghosh, P.; Ahmed, I.; Chakraborty, M.; Naiya, G.; Ghosh, B. Constrained α-Helical Peptides as Inhibitors of Protein-Protein and Protein-DNA Interactions. *Biomedicines* **2018**, *6* (4), 118. DOI: ARTN 118 10.3390/biomedicines6040118. Vaughn, J. P.; Creacy, S. D.; Routh, E. D.; Joyner-Butt, C.; Jenkins, G. S.; Pauli, S.; Nagamine, Y.; Akman, S. A. The DEXH protein product of the DHX36 gene is the major source of tetramolecular quadruplex G4-DNA resolving activity in HeLa cell lysates. *J Biol Chem* **2005**, *280* (46), 38117-38120. DOI: 10.1074/jbc.C500348200.

(20) Park, B.; Lim, J. K.; Shin, K. M.; Hong, J.; Cha, J. G.; Cho, S. H.; Park, S. Y.; Ryeom, H. K.; Kim, S. H.; Seo, A. N.; et al. Clinical Role of Upfront F-18 FDG PET/CT in Determining Biopsy Sites for Lung Cancer Diagnosis. *Diagnostics* **2024**, *14* (2), 153. DOI: ARTN 153 10.3390/diagnostics14020153. Mei, R.; Pyka, T.; Sari, H.; Fanti, S.; Afshar-Oromieh, A.; Giger, R.; Caobelli, F.; Rominger, A.; Alberts, I. The clinical acceptability of short versus long duration acquisitions for head and neck cancer using long-axial field-of-view PET/CT: a retrospective evaluation. *Eur J Nucl Med Mol I* **2023**, *51*, 1436-1443. DOI: 10.1007/s00259-023-06516-6. Lo, R.; Majid, A.; Fruhwirth, G. O.; Vilar, R. Radiolabelling Pt-based quadruplex DNA binders click chemistry. *Bioorgan Med Chem* **2022**, *76*, 117097. DOI: ARTN 117097 10.1016/j.bmc.2022.117097.

(21) Lee, A. C. L.; Harris, J. L.; Khanna, K. K.; Hong, J. H. A Comprehensive Review on Current Advances in Peptide Drug Development and Design. *Int J Mol Sci* **2019**, *20* (10), 2383. DOI: ARTN 2383 10.3390/ijms20102383.

(22) Yan, X. F.; Niu, G.; Wang, Z.; Yang, X. Y.; Kiesewetter, D. O.; Jacobson, O.; Shen, B. Z.; Chen, X. Y. Al[^{18}F]NOTA-T140 Peptide for Noninvasive Visualization of CXCR4 Expression. *Mol Imaging Biol* **2016**, *18* (1), 135-142. DOI: 10.1007/s11307-015-0872-2.

(23) Yaneva, M. Y.; Cheong, V. V.; Cheng, J. K.; Lim, K. W.; Phan, A. T. Stapling a G-quadruplex specific peptide. *Biochem Bioph Res Co* **2020**, *531* (1), 62-66. DOI: 10.1016/j.bbrc.2020.02.144.

(24) Laverman, P.; D'Souza, C. A.; Eek, A.; McBride, W. J.; Sharkey, R. M.; Oyen, W. J. G.; Goldenberg, D. M.; Boerman, O. C. Optimized labeling of NOTA-conjugated octreotide with F-18. *Tumor Biol* **2012**, *33* (2), 427-434. DOI: 10.1007/s13277-011-0250-x.

(25) Lighezan, L.; Georgieva, R.; Neagu, A. The secondary structure and the thermal unfolding parameters of the S-layer protein from. *Eur Biophys J Biophy* **2016**, *45* (6), 491-509. DOI: 10.1007/s00249-016-1117-2.

(26) Machireddy, B.; Kalra, G.; Jonnalagadda, S.; Ramanujachary, K.; Wu, C. Probing the Binding Pathway of BRACO19 to a Parallel-Stranded Human Telomeric G-Quadruplex Using Molecular Dynamics Binding Simulation with AMBER DNA OL15 and Ligand GAFF2 Force Fields. *J Chem Inf Model* **2017**, *57* (11), 2846-2864. DOI: 10.1021/acs.jcim.7b00287.

(27) Vergani, L.; Prescott, A. R.; Holt, I. J. Rhabdomyosarcoma ρ0 cells: isolation and characterization of a mitochondrial DNA depleted cell line with 'muscle-like' properties. *Neuromuscular Disord* **2000**, *10* (6), 454-459. DOI: Doi 10.1016/S0960-8966(00)00096-1.

(28) Gizatullina, Z. Z.; Gaynutdinov, T. M.; Svoboda, H.; Jerzembek, D.; Knabe, A.; Vielhaber, S.; Malesevic, M.; Heinze, H. J.; Fischer, G.; Striggow, F.; et al. Effects of cyclosporine A and its immunosuppressive or non-immunosuppressive derivatives [D-Ser]^{8}-CsA and Cs9 on mitochondria from different brain regions. *Mitochondrion* **2011**, *11* (3), 421-429. DOI: 10.1016/j.mito.2010.12.012.

(29) Park, K. S.; Jo, I.; Pak, Y. K.; Bae, S. W.; Rhim, H.; Suh, S. H.; Park, S. J.; Zhu, M. H.; So, I.; Kim, K. W. FCCP depolarizes plasma membrane potential by activating proton and Na^{+} currents in bovine aortic endothelial cells. *Pflug Arch Eur J Phy* **2002**, *443* (3), 344-352. DOI: DOI 10.1007/s004240100703.

(30) Giesel, F. L.; Hadaschik, B.; Cardinale, J.; Radtke, J.; Vinsensia, M.; Lehnert, W.; Kesch, C.; Tolstov, Y.; Singer, S.; Grabe, N.; et al. F-18 labelled PSMA-1007: biodistribution, radiation dosimetry and histopathological validation of tumor lesions in prostate cancer patients. *Eur J Nucl Med Mol I* **2017**, *44* (4), 678-688. DOI: 10.1007/s00259-016-3573-4.

(31) Schildt, A.; de Vries, E. F. J.; Willemsen, A. T. M.; Moraga-Amaro, R.; Lima-Giacobbo, B.; Sijbesma, J. W. A.; Sossi, V.; Dierckx, R. A. J. O.; Doorduin, J. Modeling of [^{18}F]FEOBV Pharmacokinetics in Rat Brain. *Mol Imaging Biol* **2020**, *22* (4), 931-939. DOI: 10.1007/s11307-019-01466-8.

(32) Cavanaugh, J. E.; Neath, A. A. The Akaike information criterion: Background, derivation, properties, application, interpretation, and refinements. *Wires Comput Stat* **2019**, *11* (3), 1460. DOI: ARTN e146010.1002/wics.1460.